Electronic and optical properties of Janus-like hexagonal monolayer materials of group IV-VI

Rafael Barbosa,[1] Danilo Kuritza,[1] Gabriel Perin,[1] R. H. Miwa,[2,*] R. B. Pontes,[3,†] and J. E. Padilha[4,‡]

[1]*Departamento de Física, Universidade Estadual de Maringá, 87020-900 Maringá, PR, Brazil.*

[2]*Instituto de Física, Universidade Federal de Uberlândia, C.P. 593, 38400-902 Uberlândia, MG, Brazil.*

[3]*Instituto de Física, Universidade Federal de Goiás, Campus Samambaia, 74690-900 Goiânia, GO, Brazil.*

[4]*Campus Avançado Jandaia do Sul, Universidade Federal do Paraná, 86900-000 Jandaia do Sul, PR, Brazil.*

(Received 14 October 2022; accepted 19 December 2022; published 11 January 2023)

We report *ab initio* calculations of the electronic and optical response properties of Janus-like hexagonal monolayers materials of group IV-VI. By combining phonons spectra calculations and *ab initio* molecular dynamics simulations, we verify that some two-dimensional (2D) group IV-VI hexagonal materials are dynamically unstable. Our results of electronic band structure based on both density functional theory (DFT) with Heyd-Scuseria-Ernzerhof hybrid functional (HSE) and G_0W_0 formalisms indicate that the dynamically stable materials exhibit indirect band gaps. The calculations clearly reveal that the hexagonal crystal structure of the group IV-VI monolayers plays a crucial role not only in determining the width of the band gap but also on the electron-hole screening effect, and consequently the strength of the exciton binding energy. Despite their strong binding, exciton binding energies in these nanomaterials are found to be in agreement with a 2D Mott-Wannier model. We also show that most of the stable 2D materials exhibit strong optical absorbance in the visible range, being promising materials for ultra-thin-film photovoltaic applications. Thus, our systematic analysis on electronic and optical properties of hexagonal monolayer materials of group IV-VI will complement forthcoming experimental measurements and can pave the way for technological applications of those materials.

DOI: 10.1103/PhysRevMaterials.7.014001

I. INTRODUCTION

For all advanced functional materials, in particular those at the flatland [1,2], the coupling between crystal lattice and atomic composition is responsible for the wide range of novel and unique physical and chemical properties they exhibit [3–5]. Such unprecedented properties, varying from magnetism to superconductivity, optical, thermal conductivity, charge(spin) density waves, topological, excitonic order, and electrochemical and catalytic properties, many times coexisting in a two-dimensional (2D) material, have driven a scientific revolution with unparalleled efforts dedicated to its syntheses, functionalization, and even processing [6–29].

In this sense, two-dimensional materials based on elemental group IV have been massively investigated, with graphene and its counterparts being the brightest stars of this group [30–39]. All group IV 2D honeycomb materials beyond graphene (C), i.e., silicene (Si), germanene (Ge), stanene (Sn), and plumbene (Pb), have now been synthesized [40–44]. Besides that, chemical functionalization is considered a promising route to band-gap engineering, which could enable nanoelectronics applications of these outstanding materials [45–48]. Also, elemental group IV 2D materials exhibit an electronic state of matter in which they show a quantum spin Hall effect (QSHE) due to spin-orbit coupling (SOC), which can be tuned by applying a perpendicular electric field, inducing a topological phase transition [21,49,50]. However, in graphene, due to small intrinsic SOC on the order of μeV, QSHE is difficult to observe [51,52].

The group IV atoms can be combined with other groups of the periodic table [53–58]. Thus, new 2D materials with completely new functionalities can be obtained. Recently, 2D group IV-VI semiconductors have attracted significant attention due to their low-cost, earth-abundant, environment-friendly characteristics, as well as unusual physical properties [53,56,59]. In particular, if the atoms of group IV are coupled with oxygen (O) atoms, a class of 2D oxides are created. Such oxides show fascinating capabilities and can exist in several crystal lattices and formula units [60–63]. For instance, 2D hexagonal silica (SiO_2), which is a wide band-gap semiconductor tunable by external electric field, has potential application in electronics as the thinnest gate dielectric [64–66].

Furthermore, the group IV monochalcogenides (group VI = S, Se, and Te) semiconductors family has promising properties for the development of a new generation of sensors, ion batteries, piezoelectrics, and optoelectronic, photovoltaic, and thermoelectric devices [56,59,67–71]. They can be synthesized by using cheaper routes like colloidal solutions, and have band gaps in a suitable range for photovoltaic applications. Also, they are earth abundant, low toxicity, environmentally friendly, and chemically stable [56,72].

Most of the investigations regarding the 2D group IV-VI consider only the puckered layered orthorhombic structure (similar to that of black phosphorus [55]). However, new

*hiroki@ufu.br
†pontes@ufg.br
‡jose.padilha@ufpr.br

phases are possible and bring new perspectives for the future of this emerging 2D material class [55,57,73,74]. Thus, much work has still to be done in order to provide a deep understanding of the novel physical and chemical properties that can emerge from these materials, such as the electronic and optical properties of those systems.

Aiming to further explore the distinct properties of the atomically thin 2D materials by taking advantage of their structures, an emerging class of 2D materials, labeled Janus 2D materials, has currently attracted increasing attention. By introducing asymmetry across different atomic planes, novel and exciting physical and chemical properties can emerge compared with their counterparts [75–78].

Thus, in this work, our mail goal is to systematically characterize and investigate the still little explored optoelectronic and photocatalytic properties of the group IV-VI Janus-like hexagonal monolayer materials. By combining phonon spectra calculations and *ab initio* molecular dynamics simulations (AIMD), we verify that some 2D group IV-VI hexagonal materials are dynamically unstable. Our findings also indicate that all stable materials exhibit indirect band gap. Also, the crystal structure of these IV-VI monolayers plays a crucial role not only in determining the width of the band gap but also on the electron-hole screening effect, and consequently the strength of the exciton binding energy. The high values of the exciton binding energies presented by the monolayers, added to the electron-hole separation, due to the internal field of the material, show that those materials are promising for application in optical, photovoltaic, and photocatalytic nanodevices

II. COMPUTATIONAL METHODS

Our calculations were based on density functional theory (DFT), as implemented in the VASP code [79,80]. As conventional exchange correlation functionals underestimate the band gap of semiconductors, we used the hybrid functional of Heyd, Scuseria, and Ernzerhof (HSE06) [81,82], which gives more accurate band gaps and at the same time also accurate structural properties. The projector augmented wave potential (PAW) [83] was used to treat the ion-electron interactions with a plane wave cutoff energy of 500 eV. We used 20 Å of vacuum to avoid spurious interactions with the periodic images, and also we used dipole corrections, because the Janus material presents an intrinsic internal electric dipole. The Brillouin zone is sampled with a $9 \times 9 \times 1$ $\vec{k}$-points sampling [84]. Excitonic effects are not explicitly included, so the reported band gaps are the fundamental band gaps.

The van der Waals interactions (vdW) are included by using the semiempirical D2 method [85], and together with HSE06 the lattice parameters and atomic positions for all structures are relaxed until residual forces on the atoms are smaller than 0.001 eV/Å. The major advantage of the HSE06-D2 methodology is that it includes van der Waals interactions and is internally consistent because of the capability to evaluate both atomic and electronic structure. It is worth mentioning that such vdW interactions were taken into account due to the exigency of an accurate description of chemical interactions/bondings in the study of structural stability (MD + phonons) of the considered systems. It has been shown that many systems traditionally believed to be treated well using discrete Fourier transform (DFT) without van der Waals correction are now being found to be systems in which this effect is actually critical [86–88].

After the structure optimization, we have analyzed the dynamic stability with the calculation of the phonon dispersion using the PHONOPY code [89]. The thermal stability was verified by *ab initio* molecular dynamics simulations (AIMD) at 300 K, with a time step of 1 fs using a Nose heating bath scheme [90]. Furthermore, the valence-band (VB) and conduction-band (CB) edges with respect to the vacuum level are determined by aligning the planar-averaged electrostatic potential within the layer with the vacuum region.

In order to analyze the optical properties and the excitonic effects, we started with the Kohn-Sham orbitals of DFT calculation to obtain the self-energies G_0W_0. To avoid the screening problems in low dimensions, we truncate the Coulomb interaction along the perpendicular axis. In order to verify the *e-h* interaction we solved the Bethe-Salpeter equation (BSE) [91–93] with the Tamm-Dancoff approximation [94]. The G_0W_0 and BSE calculations were performed with the YAMBO code [95]. We have been especially cautious to check the convergence of the number of k points, empty bands, as well as the size of the dielectric matrix.

III. RESULTS

A. Structural properties

We start our investigation by analyzing the crystal lattice properties of the hexagonal IV-VI Janus monolayers (JMLs), with group IV = C, Si, Ge, or Sn, and group VI = O, S, Se, or Te atoms. The structural model of IV-VI JML can be be regarded as two interleaving triangular lattices, where each atom in one sublattice *A* has three nearest neighbors in sublattice *B* and vice versa. For instance, we can consider group IV atoms composing the sublattice *A* and group VI atoms in sublattice *B* and vice versa. In Fig. 1(a) we present the top and side views in a ball-and-stick representation of a hexagonal JML, and the key structural information is summarized in Table I.

Our results of equilibrium geometry agree well with those presented in previous Perdew-Burke-Ernzerhof (PBE)–DFT calculations [55,74,96–98]. For instance, the lattice parameters of 3.718 and 3.548 Å for GeS and GeSe JMLs, respectively, compare very well with those presented in Refs. [96,98]. In addition, we found that instead of the planar sp^2 hybridization characteristic of graphene, the energetic preference for sp^3 hybridization dictates the formation of buckled hexagonal IV-VI JMLs, with the triangular lattices *A* and *B* vertically separated by *h* [Fig. 1(a)]. It is worth noting that, as shown in Table I, both quantities, the equilibrium lattice constant and vertical buckling, follow the increase of the atomic radius of both (groups IV and VI) elements. Recent total energy results indicate that the IV-VI puckered and buckled JMLs are energetically stable [55], with the tetragonal puckered structure being more stable than the hexagonal JML. However, further investigations are necessary in order to examine the dynamical and structural stability of these hexagonal IV-VI JMLs.

We have examined the dynamical stability of the IV-VI JMLs through the simulation of phonon spectra. Figures 1(b)–

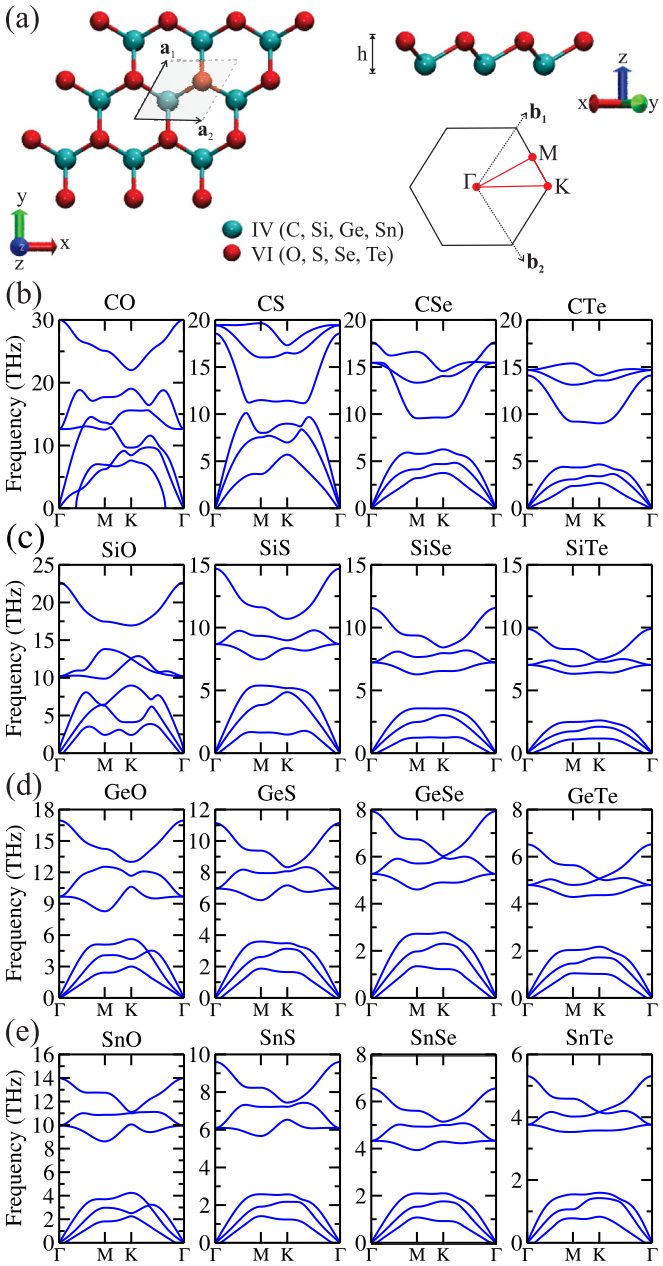

FIG. 1. (a) Top (left panel) and side (right panel) views of the ball-and-stick model of the hexagonal binary IV-VI materials (IV= C, Si, Ge, Sn; VI = O, S, Se, Te). The unit cell (shaded region) defined by the lattice vectors $\mathbf{a}_{1,2}$ and the schematic representation of the Brillouin zone, with the high symmetry points considered in the band structure calculations, are also presented. Phonon spectra for (b) CVI; (c) SiVI; (d) GeVI; and (e) SnVI

1(e) display phonon dispersion curve plots for all studied materials. For carbon-based materials (CVI), we verify that the hexagonal CO is dynamically unstable since it exhibits phonon instabilities in the low-frequency acoustic modes in the vicinity of the Γ point, suggesting that such a system cannot be realized in the free-standing form. In contrast, the other materials do not have imaginary vibrational frequencies, thus suggesting that (in principle) they could be obtained in their free-standing form.

TABLE I. Computed structural parameters of free-standing Janus hexagonal monolayer materials of group IV-VI: Lattice parameters (a), buckling heights (h), and interatomic distance between group IV and group VI elements ($d_{\mathrm{IV-VI}}$).

2D IV-VI	a (Å)	h (Å)	$d_{\mathrm{IV-VI}}$ (Å)
CO	2.341	0.761	1.551
CS	2.830	0.818	1.827
CSe	3.089	0.969	2.030
CTe	3.359	1.042	2.201
SiO	2.748	0.924	1.836
SiS	3.398	1.259	2.331
SiSe	3.612	1.337	2.477
SiTe	3.918	1.439	2.681
GeO	2.987	0.952	1.970
GeS	3.549	1.291	2.422
GeSe	3.718	1.372	2.548
GeTe	3.999	1.479	2.742
SnO	3.274	0.988	2.133
SnS	3.772	1.406	2.592
SnSe	3.904	1.509	2.714
SnTe	4.168	1.635	2.913

In the sequence, the structural stability of the JMLs was verified through a set of AIMD simulations at room temperature. We have considered with a time step of 1 fs using a Nose heating bath, for a time up to 10 ps. In Fig. 2, we show plots of the total potential energy with respect to the simulation time. Snapshots of the last configurations are also shown. We verified that, even CS [Fig. 2(a), second top panel] and all Si-based [Fig. 2(c)] materials exhibiting dynamical stability, they are not thermally stable. The hexagonal lattice is completely amorphized even at T= 300 K, whereas the other hexagonal IV-VI JMLs maintain their structural stability, namely, IV-VI monochalcogeneides [Figs. 2(a3), 2(a4), 2(c2)–2(c4), and 2(d2)–2(d4)], and IV-VI oxides, as shown in Figs. 2(c1) and 2(d1). In the next section we will focus on the electronic properties of these dynamically and structurally stable IV-VI JMLs.

B. Electronic properties

Based on the PBE–generalized-gradient approximation (GGA) approach, Kamal *et al.* [55] verified that the hexagonal GeX and SnX JMLs, with X = S, Se, and Te, present energy band gaps larger that those obtained in the orthorhombic puckered counterparts. Further HSE electronic band structure calculations of the orthorhombic puckered [99] and hexagonal buckled [96–98,100] GeS and GeSe have confirmed the larger energy band gaps in the latter geometry.

Let us start with the electronic band structures of the hexagonal GeX and SnX JMLs (X = S, Se, and Te), Figs. 3(a) and 3(b). These systems present indirect band gaps, where the lowest conduction band ($c1$) is dictated by the group IV elements; meanwhile, the topmost valence band ($v1$) is characterized by the predominance of (i) chalcogen orbitals near the center of the Brillouin zone, and (ii) Ge (less intense) and Sn (more intense) orbital contribution along the edge states of the Brillouin zone, MK direction. Our results of (HSE06

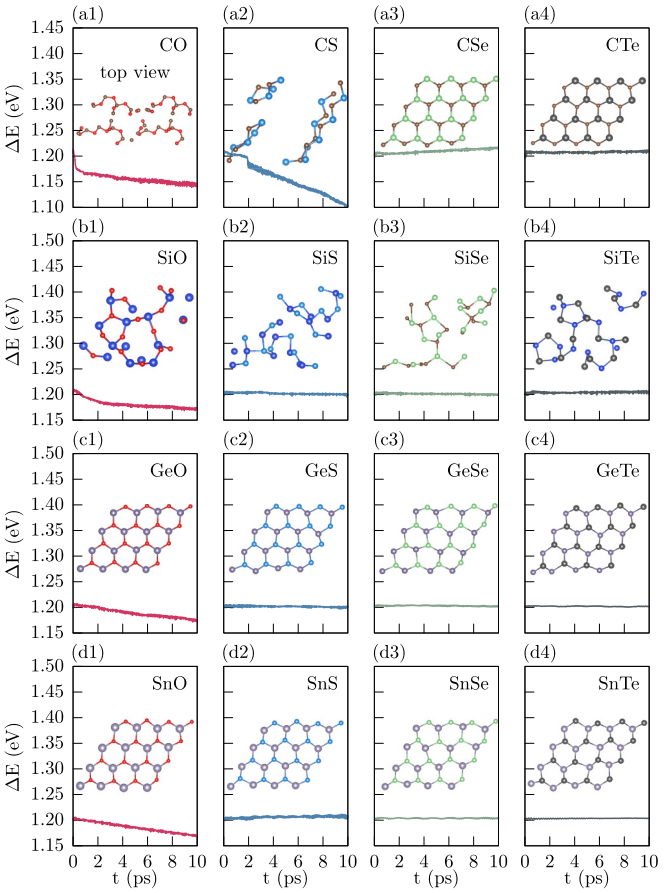

FIG. 2. (a1)–(d4)Total energy fluctuation during AIMD simulations (at 300 K) of the Janus hexagonal monolayer materials of group IV-VI. The insets are snapshots of the crystal structures at 10 ps.

TABLE II. HSE06 and G_0W_0 calculated band gaps, VBM and CBM band edge positions, and asymmetry between the two different levels of the vacuum energy (δ) for the stable hexagonal Janus monolayer materials of group IV-VI.

2D IV-VI	HSE06	G_0W_0	VBM	CBM	δ (eV)
GeS	3.26	4.13	Γ-K	M-Γ	0.73
GeSe	3.00	3.44	Γ-K	M-Γ	0.51
GeTe	2.28	3.16	Γ	M-Γ	0.24
SnS	2.97	4.05	Γ-K	M	1.06
SnSe	2.83	3.76	Γ-K	M-Γ	0.81
SnTe	2.46	3.59	Γ	M-Γ	0.51
CSe	2.05	2.58	Γ-K	M-Γ	2.46
CTe	1.70	1.99	Γ-K	M-Γ	2.25
GeO	2.71	4.22	K	M	1.09
SnO	2.08	3.29	K	M	1.26

and G_0W_0) band gaps and the localization of the valence band maximum (VBM) and conduction band minimum (CBM) are summarized in Table II. We find that the HSE06 band gaps of GeS and GeSe, 3.26 and 3.00 eV, are in good agreement with previous ones obtained at the same level of theory [96,98]. It is worth pointing out the following findings: (i) the HSE06 band gaps increase upon the inclusion of G_0W_0 (one-shot) self-energy corrections, for instance, 3.26 → 4.13 eV, 3.00 → 3.44 eV, and 2.28 → 3.16 eV in GeX with X = S, Se, and Te, respectively. Similar band-gap increase has been verified in the other IV-VI JMLs. In Ref. [99] the authors have also verified an increase of the band gaps for the orthorhombic GeS and GeSe MLs; however, they found energy differences of 0.4 and 0.09 eV, which can be attributed to the differences in the atomic arrangement of these single-layer systems. (ii) The strength of *s*-*p* hybridization between the group IV elements

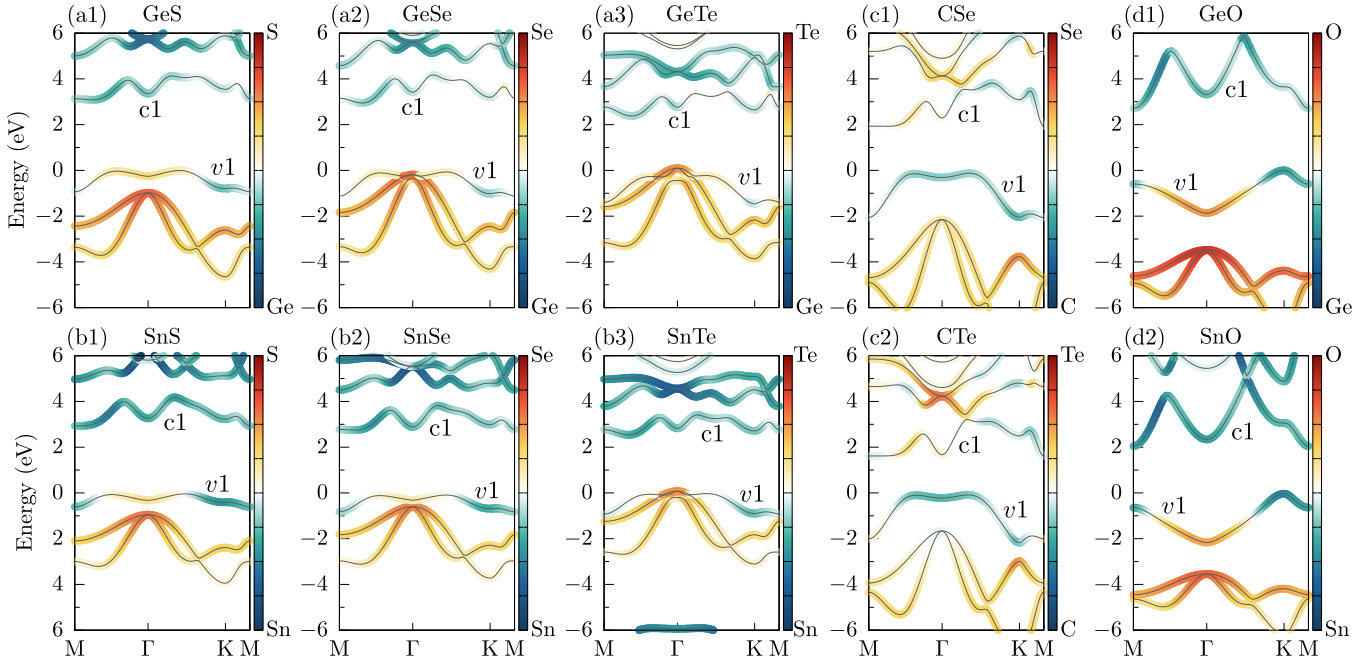

FIG. 3. Atom-resolved electronic band structures of the dynamically stable hexagonal group IV-VI materials. Zero energies were set at the VBM.

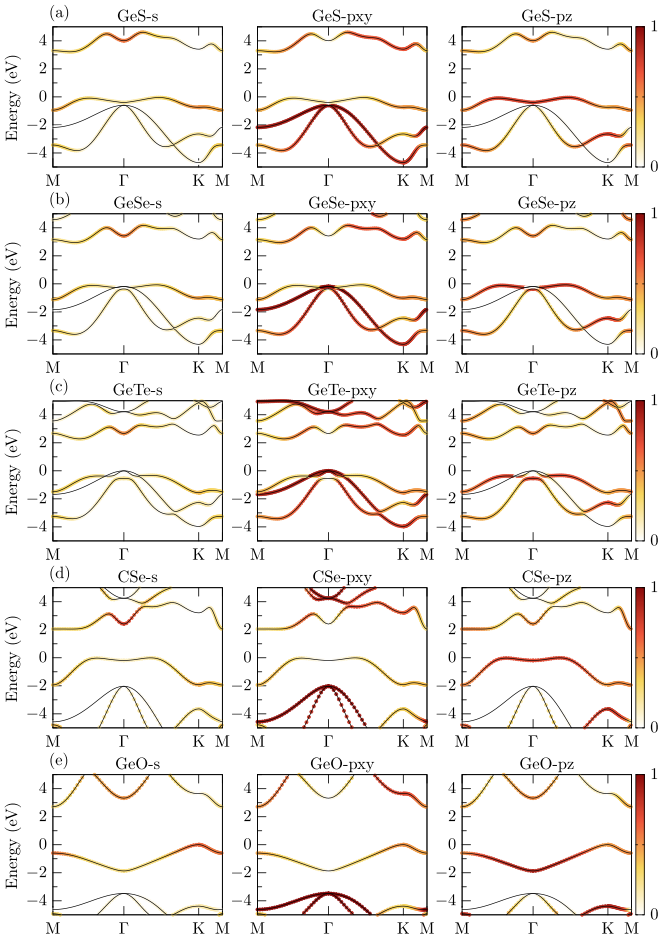

FIG. 4. Orbital projected band structure for (a) GeS, (b) GeSe, (c) GeTe, (d) CSe, and (e)GeO. The projections were made considering all elements and the s, p_{xy}, and p_z orbitals. The Fermi level was set to zero energy.

and the chalcogen atom rules the width of the band gap, which in turn is inversely proportional to the equilibrium lattice constant of the JMLs. Indeed, as shown in Table II, there is a reduction of the HSE06 (G_0W_0) computed band gap which is proportional to the size of atomic radii (R) of the chalcogen atoms, namely, $R_S < R_{Se} < R_{Te}$, and the equilibrium lattice constant of the hexagonal JMLs, Table I. For instance, Sun *et al.* verified that the band gap of hexagonal JML of GeS reduces from 3.27 to 2.95 eV upon a biaxial tensile strain of 5%, very close to the band gap of the unstrained hexagonal GeSe JMLs (3.00 eV) [98], which has a lattice constant about 5% larger than that of GeS.

In Figs. 4(a)–4(c) we show the orbital contributions of the hexagonal GeS, GeSe, and GeTe JMLs; similar orbital contributions were obtained in SnX, with X = S, Se, and Te (not shown). Combining the orbital contribution depicted in Fig. 4 with the atom resolved electronic band structure, Figs. 3(a1)–3(a3), we find that near the Γ point the lowest unoccupied energy band $c1$ is composed of Ge-4s and $-4p_z$ orbitals, whereas the in-plane Ge-4p_{xy} orbitals dictate the electronic states along the ΓK and ΓM directions; in contrast, the chalcogen-p_z orbitals bring the major contribution to the highest occupied energy band ($v1$).

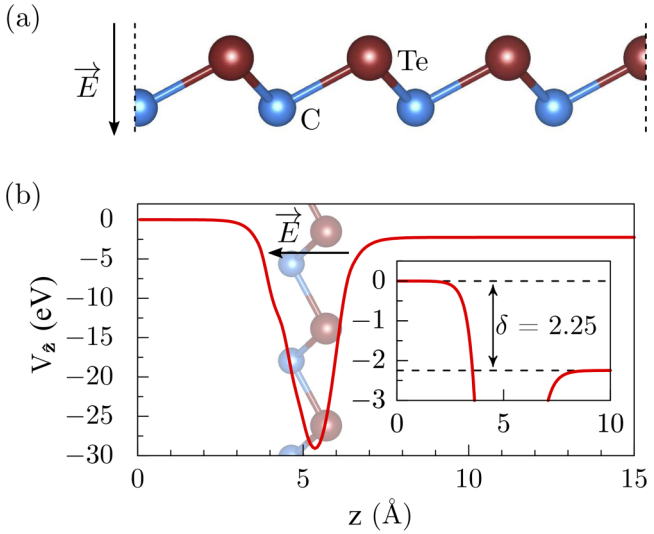

FIG. 5. (a) Direction of the driven electric field present because of the potential difference between the different sides of the material. (b) Average potential energy for CTe along the perpendicular direction to the plane of the material.

Among the IV-VI hexagonal JMLs with carbon as the group IV element, the CSe and CTe are dynamically and structurally stable (Figs. 1 and 2). The electronic band structures of these JMLs, shown in Figs. 3(c1) and 3(c2), reveal the emergence of a flat band ($v1$) mostly composed of C-2p_z orbitals [Fig. 4(d) for CSe]; similar results were obtained for CTe (not shown). Such an energy band, $v1$ is characterized by a Mexican-hat-like dispersion, giving rise to a van Hove singularity in the density of states (DOS) nearly resonant with the Fermi level. These electronic band pictures allow us to infer the emergence of a Stoner-type magnetic instability in CSe and CTe JMLs, somewhat similar to that predicted for the GeSe monolayer [101]. Focusing on the GeO and SnO JML oxides, we obtained HSE06 (G_0W_0) band gaps of 2.71 eV (4.22 eV) and 2.08 eV (3.29 eV) with the energy band $v1$ mostly composed of O-2p_z orbitals at the vicinity of the Γ point, whereas the contribution of Ge-4p_z [Fig. 4(e)] and Sn-5p_z [not shown] becomes dominant at the edge of the Brillouin zone, KM direction, and the combination of s and p states of the group IV elements dominates the conduction band $c1$, Figs. 3(d1), 3(d2), and 4(e).

Once one sublattice is composed of group IV elements and the other of group VI elements, there is a potential gradient normal to the basal plane of the 2D material, which leads to a perpendicular intrinsic electric field $\vec{E}$. The direction of $\vec{E}$ follows the difference in electronegativity originated by the different atomic species that constitute each of the sublattices. Figure 5(a) illustrates such behavior for CTe JML. In Fig. 5(b), we present the (planar) averaged electrostatic potential normal to the IV-VI layers. By comparing the energy positions of the vacuum level on both sides, plateaus on the left and right sides of the material, we find an asymmetry between the electrostatic potentials between the opposite sides (δ). In particular, for CTe we found $\delta = 2.25$ eV [Fig. 5(b) inset]. Such an intrinsic electric dipole plays an important role in the photocatalyst process in 2D platforms, which combined

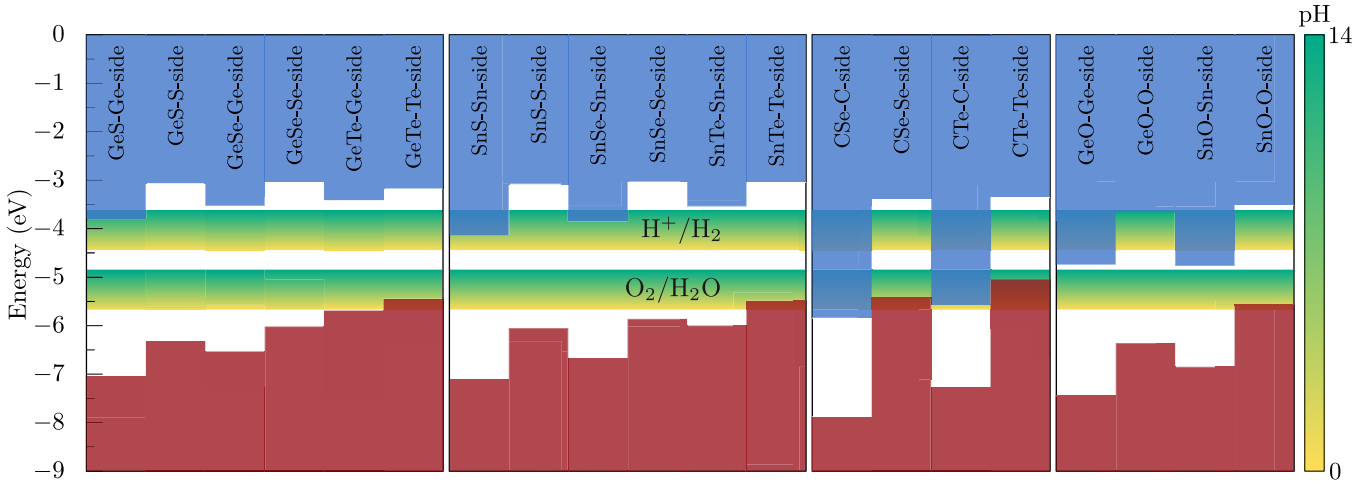

FIG. 6. Band edges for all hexagonal group IV-VI Janus materials. They are presented as aligned with respect to both sides of the materials. We also present the reduction/oxidation potential of water as a function of the pH value (green to yellow region).

with the (layer) localization of the VBM and CBM on the opposite sides of the IV-VI JML will promote a more efficient separation of the photogenerated electron-hole pairs, thus reducing the rate of electron-hole recombination. Consequently, the exciton lifetime in Janus structures is significantly longer than in their pristine counterparts, making these materials useful for photovoltaic and photodetection applications [96,98,102,103].

Focusing on efficient hydrogen generation by photocatalytic water split, in addition to the reduction of the electron-hole recombination rate, the energy position of the CBM and VBM should be higher and lower than the reduction level of hydrogen (H^+/H_2) and the oxidation level of oxygen (O_2/H_2O), respectively. In Fig. 6 we present a side-dependent energy map of the ionization potentials (IP), electron affinity (EA), and the (HSE06) band gaps of the IV-VI JMLs, combined with the energy range of the redox potentials as a function of pH. We find the following: (i) The GeX and SnX, with X = S, Se, and Te, JMLs fulfill the conditions above to be good photocatalyst materials, where the redox reaction may take place on both sides of the JMLs. (ii) In CSe and CTe, the redox reaction occurs only on the chalcogen face on the JMLs, with the oxidation reaction in CTe constrained to a higher values of pH. In the JML oxides, GeO and SnO, we find that the redox reaction will occur on the oxygen side. Finally, it is worth noting that in (ii), the larger values of δ, see Table II, will promote in a more effective separation the photogenerated electron-hole pairs.

C. Optical properties

Excitonic effects are quite an important issue in the optical properties of materials, both from a fundamental aspect as well as from the perspective of technological applications. In this last subsection, we will focus on the role played by the electron-hole (*e-h*) Coulombic interaction on the optical absorption spectra, the direct- and reciprocal-space localization of the excitonic states in the the group IV-VI 2D systems, and the suitability of these JMLs in photocatalytic processes.

The optical absorption spectra are determined by the imaginary part of the macroscopic dielectric function (Im ε_2). Here, we have considered the G_0W_0-Random Phase Approximation (RPA) (without the *e-h* interaction) and G_0W_0-BSE (excitonic effects included) approaches to calculate the imaginary parts of the dielectric functions. Our results of absorption spectra as a function of the photon energy, depicted in Fig. 7, reveal that the *e-h* interactions modify dramatically the optical spectra profile. For all stable materials, the excitonic absorption edges are red-shifted and the spectrum profile is completely different compared to the G_0W_0-RPA spectrum, with a main increase in its relative absorption intensity.

In addition, as show in Fig. 7, we find that hexagonal group IV-VI JMLs show good ability to absorb light in the visible and near-infrared (NIR) regions, which is evident from the high absorption peaks at approximately 1.87 and 3.14 eV in the visible region of their respective spectra. As shown in Figs. 7(a) and 7(b), GeX and SnX JMLs (X = chalcogen atoms) present their first absorption peak near 3.0 eV. Similar results for GeSe (3.00 eV) and SnS (3.03 eV) have been found in Refs. [97,98]. Meanwhile, as depicted in Fig. 7(c1), the CSe JML present the first absorption peak for photon energy at about 1.8 eV, which is quite interesting for applications in photocatalysis. Since the wavelengths of light arriving on earth are mainly in the visible and NIR regions, these findings suggest that such 2D materials are promising components for various optical, photovoltaic, and photocatalytic applications.

In general, due to the reduced screening, the exciton binding energy (E^b) in 2D materials are larger than that of their three-dimensional (3D) counterparts [104,105]. E^b is defined as the difference between the exciton's energy and the energy of dominant band-to-band transition, where the lowest energy direct transition occurs. In Table III, we present the energy positions and binding energies of the first excitonic peak. In GeX (SnX) JMLs, we found E^b between 1.20 and 0.70 eV (1.26–0.95 eV) for X = S, Se, and Te, respectively, suggesting that the electronic screening effects are inversely proportional to the electronegativity of the chalcogen atom. It is worth noting that the same screening dependence has been verified

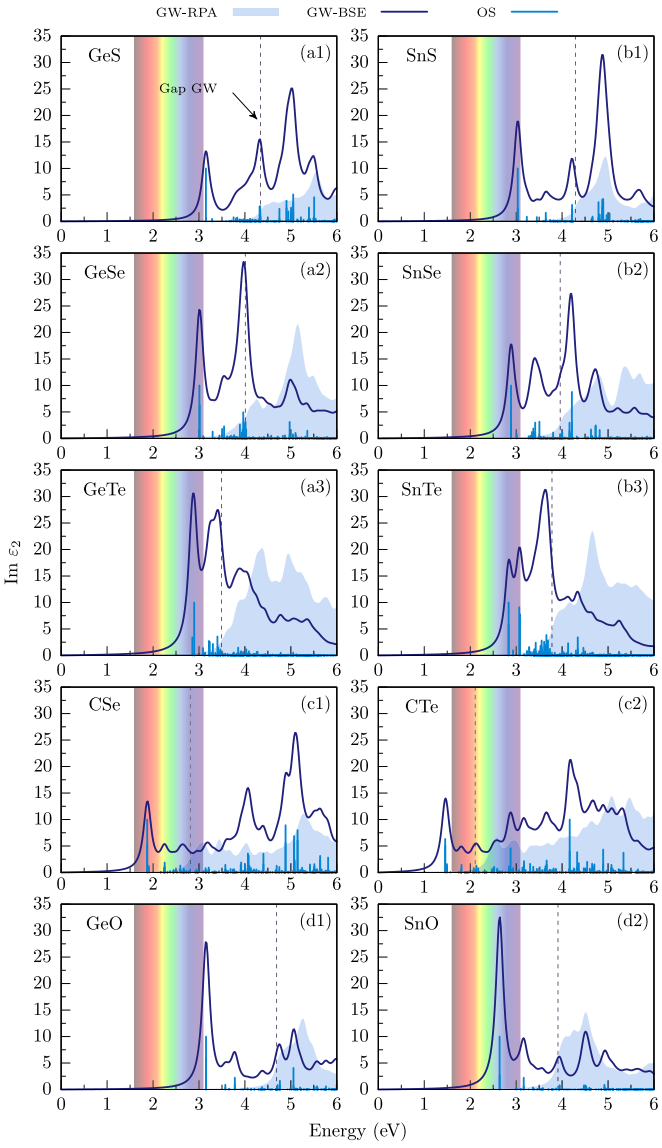

FIG. 7. Imaginary part of the dielectric function calculated with G_0W_0 and G_0W_0 + BSE and the relative oscillator strength of individual excitonic states (blue bars) for dynamically and thermally stable hexagonal group IV-VI materials. The black dashed lines indicate the G_0W_0 band gaps.

TABLE III. Energies (G_0W_0-BSE and G_0W_0-RPA) and binding energies (in eV) of the first excitonic peak E_b and binding energy Mott-Wannier (E_b^{MW}).

2D IV-VI	E^{BSE} (eV)	E^{RPA} (eV)	E_b (eV)	E_b^{MW}
GeS	3.14	4.34	1.20	1.37
GeSe	3.00	4.01	1.01	0.88
GeTe	2.87	3.57	0.70	0.56
SnS	3.03	4.29	1.26	1.72
SnSe	2.88	3.96	1.08	1.12
SnTe	2.83	3.78	0.95	0.98
CSe	1.87	2.81	0.94	0.61
CTe	1.45	2.11	0.66	0.48
GeO	3.14	4.69	1.55	2.93
SnO	2.64	3.91	1.27	2.39

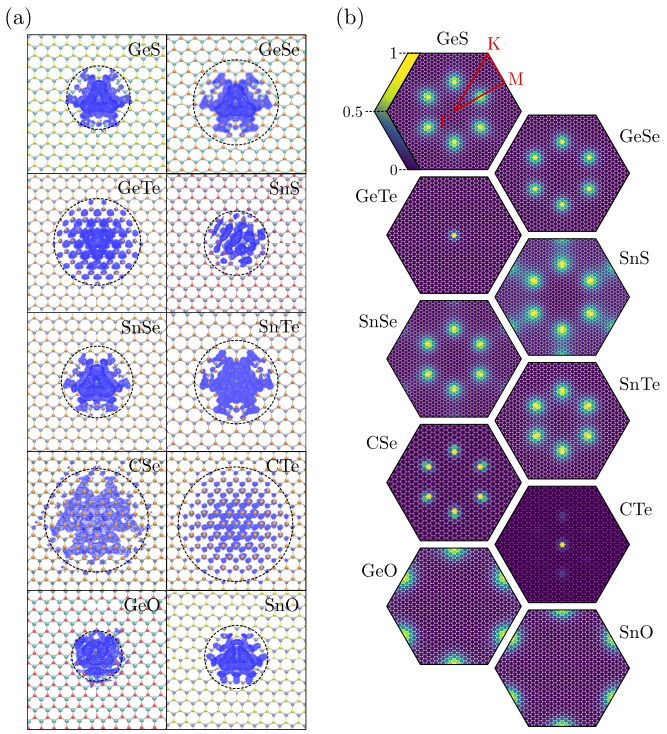

FIG. 8. (a) Real and (b) $\vec{k}$-space distribution of the squared amplitude of first bright exciton wave functions of the hexagonal group IV-VI Janus monolayers.

for their (tetragonal) puckered counterparts, GeS, GeSe, and SnSe MLs. However, those puckered systems present lower values of exciton binding energies, i.e., $E^b = 1.05$ eV, 0.4 eV, and 0.27 eV [99,106], respectively, indicating that the crystal structure of the IV-VI monolayers plays a crucial role not only in determining the width of the band gap but also on the electron-hole screening effect, and consequently the strength of the exciton binding energy. Moreover, we found that the oxide JMLs, GeO and SnO, present larger values of E^b, where the latter is comparable with that of SnS, while the former presents the largest value of exciton binding energy, 1.55 eV.

Aiming to deepen the discussion about excitons, in Fig. 8 we show the real- and reciprocal-space distribution of the normalized squared wave function of the first exciton peak ($|\psi_{1,\mathbf{k}}|^2$). Let us start with the GeX and SnX JMLs. The real-space localization of $|\psi_{1,\mathbf{k}}|^2$ is in consonance with the smallest/largest screening effect of the more/less electronegative sulfur/tellurium atom. For instance, in GeS (SnS) the *e-h* wave function localizes within a region of about 12 (11) unit cells, whereas in GeTe (SnTe) $|\psi_{1,\mathbf{k}}|^2$ spreads out through about 22 (16) unit cells. Meanwhile, the reciprocal-space diagram reveals that $\psi_{1,\mathbf{k}}$ comes from the transition between $v1$ and $c1$ for wave vectors $\mathbf{k}$ lying between Γ and M, with an exception for GeTe, where the first excitonic state is due to the wave functions at the center of the Brillouin zone, $\mathbf{k} = 0$. Although the larger values of exciton binding energies, the real-space localization of $|\psi_{1,\mathbf{k}}|^2$ suggests the emergence of Mott-Wannier excitons. In order to provide a quantitative picture of the nature of the excitons, we have calculated the exciton binding energies by means of the semiclassical

TABLE IV. Effective mass of electrons (e) and holes (h) m_i^* ($i = h,\ e$), the scaled reduced effective mass (η^*), and the dielectric constant (ϵ).

2D IV-VI	m_h^*	m_e^*	η^*	ϵ
CSe	1.51	0.16	0.14	3.60
CTe	1.22	0.14	0,12	3.80
GeO	1.16	0.44	0.31	2.43
GeS	2.04	0.22	0.20	2.83
GeSe	1.66	0.19	0.17	3.27
GeTe	0.53	0.22	0.15	3.93
SnO	0.76	0.60	0.33	2.79
SnS	0.91	0.40	0.27	2.96
SnSe	2.14	0.23	0.21	3.16
SnTe	0.66	0.37	0.23	3.61

Mott-Wannier theory (E_b^{MW}). Such a 2D MW method was successfully employed in other Janus materials (with a built-in dipole moment) [107]. In the strictly 2D limit, the MW binding energy equation for the ground state is [108]

$$E_0 = \frac{\eta e^4}{8(\epsilon h)^2} = \frac{\eta^*}{\epsilon_r^2}\frac{m_o e^4}{8(\epsilon_0 h)^2} \approx \frac{\eta^*}{\epsilon_r^2} \times 13\,605\ \mathrm{eV} \quad (1)$$

$$E_{\mathrm{MW}}^{\mathrm{2D}} = 4E_0, \quad (2)$$

where $\eta = \frac{m_e^* m_h^*}{m_e^* + m_h^*}$ and $\eta^* = \frac{1}{m_o}\left(\frac{m_e^* m_h^*}{m_e^* + m_h^*}\right)$ are the reduced effective mass and the scaled reduced effective mass of the electron-hole pair, respectively. The effective mass m_i^* [$i =$ holes (h), electrons (e)] is determined by the curvature of the energy band edge at the optical transition between VBM and CBM, and ϵ_r is the static in-plane dielectric constant. The calculated values for $m_{h,e}^*$, η^*, and ϵ can be seen in Table IV.

Our results of exciton binding energies through the semiclassical $E_{\mathrm{MW}}^{\mathrm{2D}}$ in Table III are in (general) good agreement with those obtained using the G_0W_0-BSE, E^b, thus confirming the Mott-Wannier character of the excitons in GeX, SnX, and CX JMLs. We find an exception for the oxides GeO and SnO. In this case, although the wave functions of the first exciton peak, $\psi_{1,\mathbf{k}}$, spread out over about 7 and 11 unit cells [Fig. 8(a)], the semiclassical model results in binding energies almost two times larger than those obtained through G_0W_0-BSE; this occurs due to difficulty in obtaining an accurate value for dielectric constant in such materials.

IV. CONCLUSIONS

In conclusion, by combining phonon spectra calculations and *ab initio* molecular dynamics simulations, we show that some 2D Janus-like hexagonal group IV-VI materials are dynamically unstable in their free-standing form. Our findings also reveal, for both DFT-HSE06 and G_0W_0 formalisms, that the dynamically stable 2D group IV-VI materials exhibit indirect electronic band gaps. The calculations of absorption spectra as a function of the photon energy reveal that the *e-h* interactions modify dramatically the optical spectra profile. In addition, we find that hexagonal group IV-VI JMLs show good ability to absorb light in the visible and NIR regions, which is evident from the high absorption peaks at approximately 1.87 and 3.14 eV in the visible region of their respective spectra. Furthermore, the calculations show the existence of strongly bound Mott-Wannier excitons in these materials. Finally, the obtained results clearly indicate that the crystal structure of the IV-VI monolayers plays a crucial role not only in determining the width of the band gap but also on the electron-hole screening effect, and consequently the strength of the exciton binding energy. Thus, these findings suggest that such 2D materials have great potential for application in optical, photovoltaic, and photocatalytic devices.

ACKNOWLEDGMENTS

This work was financially supported by the Brazilian agencies FAPEG, FAPEMIG, and INCT/CNPq. We would like to acknowledge computing time provided by CENAPAD-SP and the National Laboratory for Scientific Computing (LNCC/MCTI) for providing HPC resources of the SDumont supercomputer (Project ltmsnano2d).

[1] P. Miró, M. Audiffred, and T. Heine, An atlas of two-dimensional materials, Chem. Soc. Rev. **43**, 6537 (2014).

[2] S. Z. Butler, S. M. Hollen, L. Cao, Y. Cui, J. A. Gupta, H. R. Gutiérrez, T. F. Heinz, S. S. Hong, J. Huang, A. F. Ismach, E. Johnston-Halperin, M. Kuno, V. V. Plashnitsa, R. D. Robinson, R. S. Ruoff, S. Salahuddin, J. Shan, L. Shi, M. G. Spencer, M. Terrones *et al.*, Progress, challenges, and opportunities in two-dimensional materials beyond graphene, ACS Nano **7**, 2898 (2013).

[3] A. McCreary, O. Kazakova, D. Jariwala, and Z. Y. A. Balushi, An outlook into the flat land of 2D materials beyond graphene: Synthesis, properties and device applications, 2D Mater. **8**, 013001 (2020).

[4] A. Gupta, T. Sakthivel, and S. Seal, Recent development in 2D materials beyond graphene, Prog. Mater. Sci. **73**, 44 (2015).

[5] G. R. Bhimanapati, Z. Lin, V. Meunier, Y. Jung, J. Cha, S. Das, D. Xiao, Y. Son, M. S. Strano, V. R. Cooper, L. Liang, S. G. Louie, E. Ringe, W. Zhou, S. S. Kim, R. R. Naik, B. G. Sumpter, H. Terrones, F. Xia, Y. Wang *et al.*, Recent advances in two-dimensional materials beyond graphene, ACS Nano **9**, 11509 (2015).

[6] N. Sethulakshmi, A. Mishra, Ajayan, Y. Kawazoe, A. K. Roy, A. K. Singh, and C. S. Tiwary, Magnetism in two-dimensional materials beyond graphene, Mater. Today **27**, 107 (2019).

[7] L. Thiel, Z. Wang, M. A. Tschudin, D. Rohner, I. Gutiérrez-Lezama, N. Ubrig, M. Gibertini, E. Giannini, A. F. Morpurgo, and P. Maletinsky, Probing magnetism in 2D materials at the nanoscale with single-spin microscopy, Science **364**, 973 (2019).

[8] A. Chaves, J. G. Azadani, H. Alsalman, D. R. da Costa, R. Frisenda, A. J. Chaves, S. H. Song, Y. D. Kim, D. He, J. Zhou,

A. Castellanos-Gomez, F. M. Peeters, Z. Liu, C. L. Hinkle, S.-H. Oh, D. Ye, S. J. Koester, Y. H. Lee, P. Avouris, X. Wang *et al.*, Bandgap engineering of two-dimensional semiconductor materials, npj 2D Mater. Appl. **4**, 29 (2020).

[9] V. P. Ningrum, B. Liu, W. Wang, Y. Yin, Y. Cao, C. Zha, H. Xie, X. Jiang, Y. Sun, S. Qin, X. Chen, T. Qin, C. Zhu, L. Wang, and W. Huang, Recent advances in two-dimensional magnets: Physics and devices towards spintronic applications, Research **2020**, 1768918 (2020).

[10] Y. Saito, T. Nojima, and Y. Iwasa, Highly crystalline 2D superconductors, Nat. Rev. Mater. **2**, 16094 (2016).

[11] B. Behera, B. C. Sutar, and N. R. Pradhan, Recent progress on 2D ferroelectric and multiferroic materials, challenges, and opportunity, Emergent Mater. **4**, 847 (2021).

[12] D. Qiu, C. Gong, S. Wang, M. Zhang, C. Yang, X. Wang, and J. Xiong, Recent advances in 2D superconductors, Adv. Mater. **33**, 2006124 (2021).

[13] Q. Ma, G. Ren, K. Xu, and J. Z. Ou, Tunable optical properties of 2D materials and their applications, Adv. Opt. Mater. **9**, 2001313 (2021).

[14] Z. Sun, A. Martinez, and F. Wang, Optical modulators with 2D layered materials, Nat. Photonics **10**, 227 (2016).

[15] J. You, S. Bongu, Q. Bao, and N. Panoiu, Nonlinear optical properties and applications of 2D materials: Theoretical and experimental aspects, Nanophotonics **8**, 63 (2019).

[16] H. Song, J. Liu, B. Liu, J. Wu, H.-M. Cheng, and F. Kang, Two-dimensional materials for thermal management applications, Joule **2**, 442 (2018).

[17] M.-J. Lee, J.-H. Ahn, J. H. Sung, H. Heo, S. G. Jeon, W. Lee, J. Y. Song, K.-H. Hong, B. Choi, S.-H. Lee, and M.-H. Jo, Thermoelectric materials by using two-dimensional materials with negative correlation between electrical and thermal conductivity, Nat. Commun. **7**, 12011 (2016).

[18] D. Li, Y. Gong, Y. Chen, J. Lin, Q. Khan, Y. Zhang, Y. Li, H. Zhang, and H. Xie, Recent progress of two-dimensional thermoelectric materials, Nano-Micro Lett. **12**, 36 (2020).

[19] D. Culcer, A. C. Keser, Y. Li, and G. Tkachov, Transport in two-dimensional topological materials: Recent developments in experiment and theory, 2D Mater. **7**, 022007 (2020).

[20] K. Choudhary, K. F. Garrity, J. Jiang, R. Pachter, and F. Tavazza, Computational search for magnetic and non-magnetic 2D topological materials using unified spin–orbit spillage screening, npj Comput. Mater. **6**, 49 (2020).

[21] J. Haruyama, Quantum-spin-Hall phases and 2D topological insulating states in atomically thin layers, J. Appl. Phys. **129**, 090902 (2021).

[22] X. Qian, J. Liu, L. Fu, and J. Li, Quantum spin Hall effect in two-dimensional transition metal dichalcogenides, Science **346**, 1344 (2014).

[23] T. Mueller and E. Malic, Exciton physics and device application of two-dimensional transition metal dichalcogenide semiconductors, npj 2D Mater. Appl. **2**, 29 (2018).

[24] P. Rivera, K. L. Seyler, H. Yu, J. R. Schaibley, J. Yan, D. G. Mandrus, W. Yao, and X. Xu, Valley-polarized exciton dynamics in a 2D semiconductor heterostructure, Science **351**, 688 (2016).

[25] X. Xi, L. Zhao, Z. Wang, H. Berger, L. Forró, J. Shan, and K. F. Mak, Strongly enhanced charge-density-wave order in monolayer $NbSe_2$, Nat. Nanotechnol. **10**, 765 (2015).

[26] H. Ryu, Y. Chen, H. Kim, H.-Z. Tsai, S. Tang, J. Jiang, F. Liou, S. Kahn, C. Jia, A. A. Omrani, J. H. Shim, Z. Hussain, Z.-X. Shen, K. Kim, B. I. Min, C. Hwang, M. F. Crommie, and S.-K. Mo, Persistent charge-density-wave order in single-layer $TaSe_2$, Nano Lett. **18**, 689 (2018).

[27] R. Bianco, I. Errea, L. Monacelli, M. Calandra, and F. Mauri, Quantum enhancement of charge density wave in NbS2 in the two-dimensional limit, Nano Lett. **19**, 3098 (2019).

[28] N. Karmodak and O. Andreussi, Catalytic activity and stability of two-dimensional materials for the hydrogen evolution reaction, ACS Energy Lett. **5**, 885 (2020).

[29] D. Deng, K. S. Novoselov, Q. Fu, N. Zheng, Z. Tian, and X. Bao, Catalysis with two-dimensional materials and their heterostructures, Nat. Nanotechnol. **11**, 218 (2016).

[30] A. K. Geim and K. S. Novoselov, The rise of graphene, Nat. Mater. **6**, 183 (2007).

[31] A. K. Geim, Graphene: Status and prospects, Science **324**, 1530 (2009).

[32] A. H. Castro Neto, F. Guinea, N. M. R. Peres, K. S. Novoselov, and A. K. Geim, The electronic properties of graphene, Rev. Mod. Phys. **81**, 109 (2009).

[33] X. Yu, H. Cheng, M. Zhang, Y. Zhao, L. Qu, and G. Shi, Graphene-based smart materials, Nat. Rev. Mater. **2**, 17046 (2017).

[34] F. Bonaccorso, Z. Sun, T. Hasan, and A. C. Ferrari, Graphene photonics and optoelectronics, Nat. Photonics **4**, 611 (2010).

[35] D. C. Elias, R. R. Nair, T. M. G. Mohiuddin, S. V. Morozov, Blake, M. P. Halsall, A. C. Ferrari, D. W. Boukhvalov, M. I. Katsnelson, A. K. Geim, and K. S. Novoselov, Control of graphene's properties by reversible hydrogenation: Evidence for graphane, Science **323**, 610 (2009).

[36] Y. Cao, V. Fatemi, S. Fang, K. Watanabe, T. Taniguchi, E. Kaxiras, and P. Jarillo-Herrero, Unconventional superconductivity in magic-angle graphene superlattices, Nature (London) **556**, 43 (2018).

[37] T. Cao, F. Zhao, and S. G. Louie, Topological Phases in Graphene Nanoribbons: Junction States, Spin Centers, and Quantum Spin Chains, Phys. Rev. Lett. **119**, 076401 (2017).

[38] O. Gröning, S. Wang, X. Yao, C. A. Pignedoli, G. Borin, C. Daniels, A. Cupo, V. Meunier, X. Feng, A. Narita, K. Müllen, Ruffieux, and R. Fasel, Engineering of robust topological quantum phases in graphene nanoribbons, Nature (London) **560**, 209 (2018).

[39] V. Meunier, A. G. Souza Filho, E. B. Barros, and M. S. Dresselhaus, Physical properties of low-dimensional sp^2-based carbon nanostructures, Rev. Mod. Phys. **88**, 025005 (2016).

[40] P. Vogt, De Padova, C. Quaresima, J. Avila, E. Frantzeskakis, M. C. Asensio, A. Resta, B. Ealet, and G. Le Lay, Silicene: Compelling Experimental Evidence for Graphenelike Two-Dimensional Silicon, Phys. Rev. Lett. **108**, 155501 (2012).

[41] J. Yuhara, B. He, N. Matsunami, M. Nakatake, and G. Le Lay, Graphene's latest cousin: Plumbene epitaxial growth on a "nano watercube," Adv. Mater. **31**, 1901017 (2019).

[42] J. Deng, B. Xia, X. Ma, H. Chen, H. Shan, X. Zhai, B. Li, A. Zhao, Y. Xu, W. Duan, S.-C. Zhang, B. Wang, and J. G. Hou, Epitaxial growth of ultraflat stanene with topological band inversion, Nat. Mater. **17**, 1081 (2018).

[43] M. E. Dávila, L. Xian, S. Cahangirov, A. Rubio, and G. L. Lay, Germanene: A novel two-dimensional germanium allotrope akin to graphene and silicene, New J. Phys. **16**, 095002 (2014).

[44] J. Yuhara and G. L. Lay, Beyond silicene: Synthesis of germanene, stanene and plumbene, Jpn. J. Appl. Phys. **59**, SN0801 (2020).

[45] P. Luo, F. Zhuge, Q. Zhang, Y. Chen, L. Lv, Y. Huang, H. Li, and T. Zhai, Doping engineering and functionalization of two-dimensional metal chalcogenides, Nanoscale Horiz. **4**, 26 (2019).

[46] Z. Liu, S. P. Lau, and F. Yan, Functionalized graphene and other two-dimensional materials for photovoltaic devices: Device design and processing, Chem. Soc. Rev. **44**, 5638 (2015).

[47] S. Lei, X. Wang, B. Li, J. Kang, Y. He, A. George, L. Ge, Y. Gong, P. Dong, Z. Jin, G. Brunetto, W. Chen, Z.-T. Lin, R. Baines, D. S. Galvão, J. Lou, E. Barrera, K. Banerjee, R. Vajtai, and P. Ajayan, Surface functionalization of two-dimensional metal chalcogenides by Lewis acid–base chemistry, Nat. Nanotechnol. **11**, 465 (2016).

[48] L. Daukiya, M. Nair, M. Cranney, F. Vonau, S. Hajjar-Garreau, D. Aubel, and L. Simon, Functionalization of 2D materials by intercalation, Prog. Surf. Sci. **94**, 1 (2019).

[49] M. Kim, C. H. Kim, H.-S. Kim, and J. Ihm, Topological quantum phase transitions driven by external electric fields in Sb2Te3 thin films, Proc. Natl. Acad. Sci. **109**, 671 (2012).

[50] Q. Liu, X. Zhang, L. B. Abdalla, A. Fazzio, and A. Zunger, Switching a normal insulator into a topological insulator via electric field with application to phosphorene, Nano Lett. **15**, 1222 (2015).

[51] C. L. Kane and E. J. Mele, Quantum Spin Hall Effect in Graphene, Phys. Rev. Lett. **95**, 226801 (2005).

[52] Y. Yao, F. Ye, X.-L. Qi, S.-C. Zhang, and Z. Fang, Spin-orbit gap of graphene: First-principles calculations, Phys. Rev. B **75**, 041401(R) (2007).

[53] C. Chowdhury, S. Karmakar, and A. Datta, Monolayer group IV-VI monochalcogenides: Low-dimensional materials for photocatalytic water splitting, J. Phys. Chem. C **121**, 7615 (2017).

[54] C.-H. Ho, W.-Y. Lin, L.-C. Chao, K.-Y. Lee, J. Inagaki, and H.-C. Hsueh, Study of structural, thermoelectric, and photoelectric properties of layered tin monochalcogenides SnX (X = S, Se) for energy application, ACS Appl. Energy Mater. **3**, 4896 (2020).

[55] C. Kamal, A. Chakrabarti, and M. Ezawa, Direct band gaps in group IV-VI monolayer materials: Binary counterparts of phosphorene, Phys. Rev. B **93**, 125428 (2016).

[56] P. D. Antunez, J. J. Buckley, and R. L. Brutchey, Tin and germanium monochalcogenide IV-VI semiconductor nanocrystals for use in solar cells, Nanoscale **3**, 2399 (2011).

[57] Q. Xie, J. Yuan, N. Yu, L. Wang, and J. Wang, Prediction of new group IV-V-VI monolayer semiconductors based on first principle calculation, Comput. Mater. Sci. **135**, 160 (2017).

[58] J.-H. Lin, H. Zhang, X.-L. Cheng, and Y. Miyamoto, Single-layer group IV-V and group V-IV-III-VI semiconductors: Structural stability, electronic structures, optical properties, and photocatalysis, Phys. Rev. B **96**, 035438 (2017).

[59] Z. Ma, B. Wang, L. Ou, Y. Zhang, X. Zhang, and Z. Zhou, Structure and properties of phosphorene-like IV-VI 2D materials, Nanotechnology **27**, 415203 (2016).

[60] A. Seko, A. Togo, F. Oba, and I. Tanaka, Structure and Stability of a Homologous Series of Tin Oxides, Phys. Rev. Lett. **100**, 045702 (2008).

[61] A. K. Singh, B. C. Revard, R. Ramanathan, M. Ashton, F. Tavazza, and R. G. Hennig, Genetic algorithm prediction of two-dimensional group-IV dioxides for dielectrics, Phys. Rev. B **95**, 155426 (2017).

[62] F. Zhang, J. Zhu, D. Zhang, U. Schwingenschlögl, and H. N. Alshareef, Two-dimensional SnO anodes with a tunable number of atomic layers for sodium ion batteries, Nano Lett. **17**, 1302 (2017).

[63] S. A. Miller, P. Gorai, U. Aydemir, T. O. Mason, V. Stevanović, E. S. Toberer, and G. J. Snyder, SnO as a potential oxide thermoelectric candidate, J. Mater. Chem. C **5**, 8854 (2017).

[64] P. Y. Huang, S. Kurasch, J. S. Alden, A. Shekhawat, A. A. Alemi, P. L. McEuen, J. P. Sethna, U. Kaiser, and D. A. Muller, Imaging atomic rearrangements in two-dimensional silica glass: Watching silica's dance, Science **342**, 224 (2013).

[65] C. Büchner and M. Heyde, Two-dimensional silica opens new perspectives, Prog. Surf. Sci. **92**, 341 (2017).

[66] E. Gao, B. Xie, and Z. Xu, Two-dimensional silica: Structural, mechanical properties, and strain-induced band gap tuning, J. Appl. Phys. **119**, 014301 (2016).

[67] S. Karmakar, C. Chowdhury, and A. Datta, Two-dimensional group IV monochalcogenides: Anode materials for Li-ion batteries, J. Phys. Chem. C **120**, 14522 (2016).

[68] X. Li, X. Zuo, X. Jiang, D. Li, B. Cui, and D. Liu, Enhanced photocatalysis for water splitting in layered tin chalcogenides with high carrier mobility, Phys. Chem. Chem. Phys. **21**, 7559 (2019).

[69] B. Mukherjee, Y. Cai, H. R. Tan, Y. P. Feng, E. S. Tok, and C. H. Sow, NIR Schottky photodetectors based on individual single-crystalline GeSe nanosheet, ACS Appl. Mater. Interfaces **5**, 9594 (2013).

[70] L. C. Gomes, A. Carvalho, and A. H. Castro Neto, Enhanced piezoelectricity and modified dielectric screening of two-dimensional group-IV monochalcogenides, Phys. Rev. B **92**, 214103 (2015).

[71] R. Guo, X. Wang, Y. Kuang, and B. Huang, First-principles study of anisotropic thermoelectric transport properties of IV-VI semiconductor compounds SnSe and SnS, Phys. Rev. B **92**, 115202 (2015).

[72] Q. Tan, L.-D. Zhao, J.-F. Li, C.-F. Wu, T.-R. Wei, Z.-B. Xing, and M. G. Kanatzidis, Thermoelectrics with earth abundant elements: Low thermal conductivity and high thermopower in doped SnS, J. Mater. Chem. A **2**, 17302 (2014).

[73] X.-Q. Tian, J.-Y. Duan, M. Kiani, Y.-D. Wei, N. Feng, Z.-R. Gong, X.-R. Wang, Y. Du, and B. I. Yakobson, Hexagonal layered group IV-VI semiconductors and derivatives: Fresh blood of the 2D family, Nanoscale **12**, 13450 (2020).

[74] N. Fatahi, D. M. Hoat, A. Laref, S. Amirian, A. H. Reshak, and M. Naseri, 2D hexagonal SnTe monolayer: A quasi direct band gap semiconductor with strain sensitive electronic and optical properties, Eur. Phys. J. B **93**, 32 (2020).

[75] R. Li, Y. Cheng, and W. Huang, Recent progress of Janus 2D transition metal chalcogenides: From theory to experiments, Small **14**, 1802091 (2018).

[76] L. Zhang, Z. Yang, T. Gong, R. Pan, H. Wang, Z. Guo, H. Zhang, and X. Fu, Recent advances in emerging Janus two-dimensional materials: From fundamental physics to device applications, J. Mater. Chem. A **8**, 8813 (2020).

[77] R. da Silva, R. Barbosa, R. R. Mançano, N. Durães, R. B. Pontes, R. H. Miwa, A. Fazzio, and J. E. Padilha, Metal chalcogenides Janus monolayers for efficient hydrogen generation by photocatalytic water splitting, ACS Appl. Nano Mater. **2**, 890 (2019).

[78] M. Yagmurcukardes, Y. Qin, S. Ozen, M. Sayyad, F. M. Peeters, S. Tongay, and H. Sahin, Quantum properties and applications of 2D Janus crystals and their superlattices, Appl. Phys. Rev. **7**, 011311 (2020).

[79] G. Kresse and J. Furthmüller, Efficient iterative schemes for ab initio total-energy calculations using a plane-wave basis set, Phys. Rev. B **54**, 11169 (1996).

[80] G. Kresse and J. Furthmüller, Efficiency of ab-initio total energy calculations for metals and semiconductors using a plane-wave basis set, Comput. Mater. Sci. **6**, 15 (1996).

[81] J. Heyd, G. E. Scuseria, and M. Ernzerhof, Hybrid functionals based on a screened Coulomb potential, J. Chem. Phys. **118**, 8207 (2003).

[82] J. Heyd, G. E. Scuseria, and M. Ernzerhof, Erratum: "Hybrid functionals based on a screened Coulomb potential", J. Chem. Phys. **124**, 219906 (2006).

[83] G. Kresse and D. Joubert, From ultrasoft pseudopotentials to the projector augmented-wave method, Phys. Rev. B **59**, 1758 (1999).

[84] H. J. Monkhorst and J. D. Pack, Special points for Brillouin-zone integrations, Phys. Rev. B **13**, 5188 (1976).

[85] S. Grimme, Accurate description of van der Waals complexes by density functional theory including empirical corrections, J. Comput. Chem. **25**, 1463 (2004).

[86] J. R. Reimers, M. J. Ford, S. M. Marcuccio, J. Ulstrup, and N. S. Hush, Competition of van der Waals and chemical forces on gold–sulfur surfaces and nanoparticles, Nat. Rev. Chem. **1**, 0017 (2017).

[87] R. Luo, W. W. Xu, Y. Zhang, Z. Wang, X. Wang, Y. Gao, P. Liu, and M. Chen, Van der Waals interfacial reconstruction in monolayer transition-metal dichalcogenides and gold heterojunctions, Nat. Commun. **11**, 1011 (2020).

[88] S. A. Tawfik, J. R. Reimers, C. Stampfl, and M. J. Ford, Van der Waals forces control the internal chemical structure of monolayers within the lamellar materials $CuInP_2S_6$ and $CuBiP_2Se_6$, J. Phys. Chem. C **122**, 22675 (2018).

[89] A. Togo and I. Tanaka, First principles phonon calculations in materials science, Scr. Mater. **108**, 1 (2015).

[90] S. Nosé, A unified formulation of the constant temperature molecular dynamics methods, J. Chem. Phys. **81**, 511 (1984).

[91] G. Strinati, Dynamical Shift and Broadening of Core Excitons in Semiconductors, Phys. Rev. Lett. **49**, 1519 (1982).

[92] M. Rohlfing and S. G. Louie, Electron-hole excitations and optical spectra from first principles, Phys. Rev. B **62**, 4927 (2000).

[93] M. Palummo, O. Pulci, R. Del Sole, A. Marini, Hahn, W. G. Schmidt, and F. Bechstedt, The Bethe–Salpeter equation: A first-principles approach for calculating surface optical spectra, J. Phys.: Condens. Matter **16**, S4313 (2004).

[94] S. Hirata and M. Head-Gordon, Time-dependent density functional theory within the Tamm-Dancoff approximation, Chem. Phys. Lett. **314**, 291 (1999).

[95] A. Marini, C. Hogan, M. Grüning, and D. Varsano, Yambo: An ab initio tool for excited state calculations, Comput. Phys. Commun. **180**, 1392 (2009).

[96] Y. Ji, M. Yang, H. Dong, T. Hou, L. Wang, and Y. Li, Two-dimensional germanium monochalcogenide photocatalyst for water splitting under ultraviolet, visible to near-infrared light, Nanoscale **9**, 8608 (2017).

[97] H. Yang, Y. Ma, S. Zhang, H. Jin, B. Huang, and Y. Dai, GeSe@SnS: Stacked Janus structures for overall water splitting, J. Mater. Chem. A **7**, 12060 (2019).

[98] L. Sun, Y. Cui, L. Peng, J. Du, S. Wang, and Y. Huang, Two-dimensional blue-phosphorene-phase germanium monochalcogenide photocatalysts for water splitting: From ultraviolet to visible absorption, J. Catal. **373**, 67 (2019).

[99] L. C. Gomes, E. Trevisanutto, A. Carvalho, A. S. Rodin, and A. H. Castro Neto, Strongly bound Mott-Wannier excitons in GeS and GeSe monolayers, Phys. Rev. B **94**, 155428 (2016).

[100] C. Liu, S. Guan, H. Yin, W. Wan, Y. Wang, and Y. Zhang, γ-GeSe: A two-dimensional ferroelectric material with doping-induced ferromagnetism, Appl. Phys. Lett. **115**, 252904 (2019).

[101] T. Cao, Z. Li, and S. G. Louie, Tunable Magnetism and Half-Metallicity in Hole-Doped Monolayer GaSe, Phys. Rev. Lett. **114**, 236602 (2015).

[102] T. Zheng, Y.-C. Lin, Y. Yu, P. Valencia-Acuna, A. A. Puretzky, R. Torsi, C. Liu, I. N. Ivanov, G. Duscher, D. B. Geohegan, Z. Ni, K. Xiao, and H. Zhao, Excitonic dynamics in Janus MoSSe and WSSe monolayers, Nano Lett. **21**, 931 (2021).

[103] X. Li, Z. Li, and J. Yang, Proposed Photosynthesis Method for Producing Hydrogen from Dissociated Water Molecules Using Incident Near-Infrared Light, Phys. Rev. Lett. **112**, 018301 (2014).

[104] D. Y. Qiu, H. Felipe and S. G. Louie, Optical Spectrum of MoS_2: Many-Body Effects and Diversity of Exciton States, Phys. Rev. Lett. **111**, 216805 (2013).

[105] A. Chernikov, T. C. Berkelbach, H. M. Hill, A. Rigosi, Y. Li, O. B. Aslan, D. R. Reichman, M. S. Hybertsen, and T. F. Heinz, Exciton Binding Energy and Nonhydrogenic Rydberg Series in Monolayer WS_2, Phys. Rev. Lett. **113**, 076802 (2014).

[106] G. Shi and E. Kioupakis, Anisotropic spin transport and strong visible-light absorbance in few-layer SnSe and GeSe, Nano Lett. **15**, 6926 (2015).

[107] P. Wang, Y. Zong, H. Liu, H. Wen, H.-X. Deng, Z. Wei, H.-B. Wu, and J.-B. Xia, Quasiparticle band structure and optical properties of the Janus monolayer and bilayer SnSSe, J. Phys. Chem. C **124**, 23832 (2020).

[108] T. Cheiwchanchamnangij and W. R. Lambrecht, Quasiparticle band structure calculation of monolayer, bilayer, and bulk MoS_2, Phys. Rev. B **85**, 205302 (2012).